



HAL
open science

Improving accuracy reconstruction of parts through a capability study: A methodology for X-ray Computed Tomography Robotic Cell

Adrien Le Reun, Kévin Subrin, Anthony Dubois, Sebastien Garnier

► **To cite this version:**

Adrien Le Reun, Kévin Subrin, Anthony Dubois, Sebastien Garnier. Improving accuracy reconstruction of parts through a capability study: A methodology for X-ray Computed Tomography Robotic Cell. *Robotics and Autonomous Systems*, 2024, 171, pp.104564. 10.1016/j.robot.2023.104564 . hal-04329315

HAL Id: hal-04329315

<https://hal.science/hal-04329315>

Submitted on 28 Mar 2024

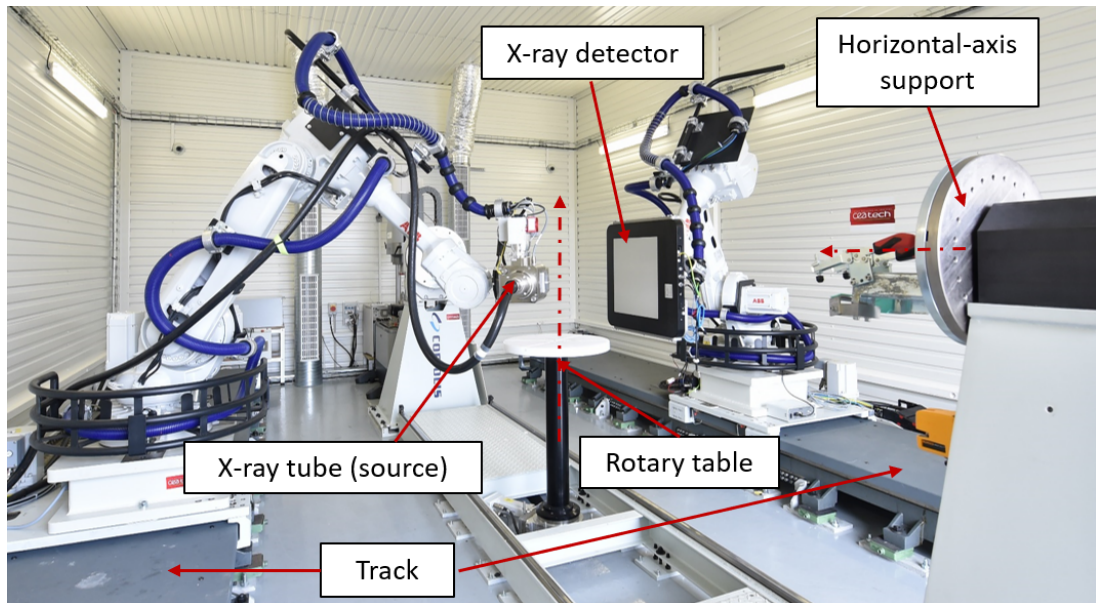
HAL is a multi-disciplinary open access archive for the deposit and dissemination of scientific research documents, whether they are published or not. The documents may come from teaching and research institutions in France or abroad, or from public or private research centers.

L'archive ouverte pluridisciplinaire **HAL**, est destinée au dépôt et à la diffusion de documents scientifiques de niveau recherche, publiés ou non, émanant des établissements d'enseignement et de recherche français ou étrangers, des laboratoires publics ou privés.

Graphical Abstract

Improving accuracy reconstruction of parts through a capability study: a methodology for X-Ray Computed Tomography Robotic Cell

Adrien Le Reun, Kevin Subrin, Anthony Dubois, Sebastien Garnier



Highlights

Improving accuracy reconstruction of parts through a capability study: a methodology for X-Ray Computed Tomography Robotic Cell

Adrien Le Reun, Kevin Subrin, Anthony Dubois, Sebastien Garnier

- Calibration of a kinematically redundant robotic cell to accurately position the X-ray source mounted on an industrial robot with respect to the detector mounted on another robot
- Development of new tools, including a large-sized test phantom and a calibration comb, to facilitate the calibration of the X-ray tomography system
- Implementation of a well-defined methodology aimed at improving the process capability for accurate part reconstruction

Improving accuracy reconstruction of parts through a capability study: a methodology for X-Ray Computed Tomography Robotic Cell

Adrien Le Reun^a, Kevin Subrin^b, Anthony Dubois^c, Sebastien Garnier^b

^a*Nantes University, Nantes University, CNRS, Laboratoire de thermique et énergie de Nantes, LTeN, UMR 6607, Nantes, 44000, France*

^b*Nantes University, Ecole Centrale Nantes, CNRS, UMR 6004, LS2N (Laboratory of Digital Sciences of Nantes), Nantes, 44000, France*

^c*CEA, CEA Tech Pays de la Loire et Bretagne, Bouguenais, 44340, France*

Abstract

Aeronautical performance is enhanced by increasingly complex and lightweight composite parts. The improvement of their manufacturing must ensure the quality measured by Non-Destructive Testing. To evaluate the health of aeronautical parts that are a few meters long, we built a high dimensional robotic cell including two industrial robots positioned on 5-meter-tracks equipped with X-Ray Computed Tomography devices. Our main objective is to reconstruct the interior of the parts and detect any anomaly that may have occurred during life cycle or manufacturing (such as porosity or inclusions). In this way, the objective is to present a methodology, firstly, to evaluate the raw process capability and secondly, to assess the improved process capability. The raw process capability uses geometrical identification and we demonstrate that without proper identification, some defects can remain hidden. Three strategies are then developed. The first one involves improving the robot behavior model, which takes into account a thermo-geometrical model, including backlash compensation. Due to possible repositioning problems and to ensure the correct knowledge of the source with respect to the detector, the second strategy involves a real-time test phantom located on the detector named the comb prototype. Finally, a large-sized steel balls phantom is designed to allow a calibration in the full workspace of the robots. This phantom is also used to accurately determine the axis of the rotary horizontal-axis support on which the large parts to be controlled are fixed. We demonstrate that such an architecture, for reconstructing a perfect sphere, leads

to an initial mean radius error of 0.05 *mm* which we improve to 0.016-0.017 *mm* with our methodology.

Keywords: X-ray computed tomography, Non-Destructive Test, robot positioning, process capability, calibration phantom, accuracy improvement

1. Introduction

The integration of industrial robots in machining, assembly and control processes has increased for decades. In aeronautics and naval industries, high dimensional parts (measuring a few meters) are numerous and need to be controlled [1]. Non-Destructive Testing (NDT) methods are used to assess material health. X-ray Computed Tomography (XCT) is a NDT volumetric control method that involves the 3D reconstruction of the inspected object [2]. Inspection enables the detection of volumetric defects such as porosity and inclusions. The quality of the reconstructed volume depends on precise knowledge of the position and orientation [3] of the X-ray source relative to X-ray detector. This aspect has been extensively studied since the work of Hashem et al. [4] which confirmed the compatibility between the tomography process and robot performance. Researchers have then turned their attention to various sources of error, such as the influence of geometrical distortion on the flat-panel detector [5]. Finally, progress is being made towards the implementation of devices to determine motion errors [6].

Existing tomography platforms [7] generally employ fixed robot(s) to hold either the source and detector or the controlled object [8] for acquiring data used in object reconstruction [9]. Based on this straightforward architecture, a circular scanning path is usually sufficient to reconstruct the part. Unfortunately, artifacts can occur and the use of a kinematically redundant robotic cell can be advantageous in facilitating access to different areas for observation by moving X-ray detector and X-ray source as shown in Figure 1 [10] [11] [12].

The resolution of reconstructed volumes can reach sub-millimeter dimensions. To achieve this, the quality of reconstruction depends mostly on a good understanding of the geometry which includes the position of the source and the position and orientation of the detector [13]. An inaccurate estimation of the true geometry can result in artifacts [4] in the reconstruction such as a contour artifact as shown in Figure 2.

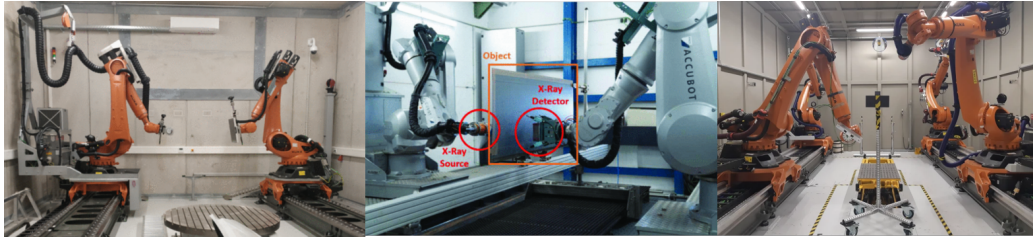
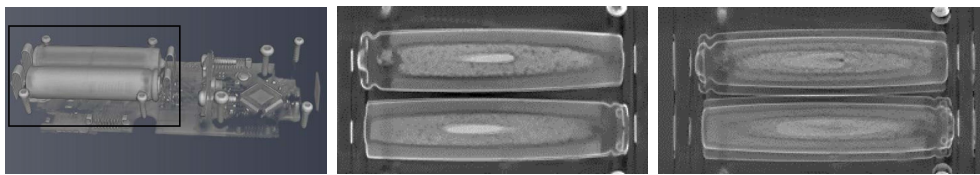


Figure 1: X-Ray CT robotic cell including industrial robots located on tracks [10] [11] [12]



(a) Reconstructed volume with accurate geometry estimation (b) Accurate geometry estimation (c) Inaccurate geometry estimation (contour artifact)

Figure 2: Contour artefact observation of two rangefinder reconstructed volumes: (a) volume and (b) slice with an accurate and (c) erroneous geometry knowledge

Driven by industrial needs, the ELIXIR platform (*CEA-Tech*) has been developed to address this issue by using two industrial 6-axes robots ABB IRB4600 (Position repeatability 0.05 mm) [14] mounted on 5-meter-tracks, each robot holds either a X-ray tube (source) and a X-ray detector (Figure 3). Additionally, one vertical and one horizontal rotation axis table can be used to position and rotate the object to be evaluated. As X-ray equipment is mounted on the robot wrist, their position directly depends on the positioning performance of the robots and the stability of their environment.

Additionally, new methods have emerged alongside standard circular tomography such as helical tomography or limited-view-angle tomography [15]. These methods applied to large parts with complex shapes involve displacements of source and detector. Moreover, the robotization of the X-ray instrumentation raises questions about the impact of robot positioning on the tomography process, *i.e* the quality of reconstruction. Trajectory optimization is then a key topic to meet process expectations. Hiller et al. [16] evaluated performance in terms of accuracy and repeatability and highlighted that the robot pose can be corrected using appropriate compensation methods. The researchers demonstrate the complexity of trajectory generation, but they

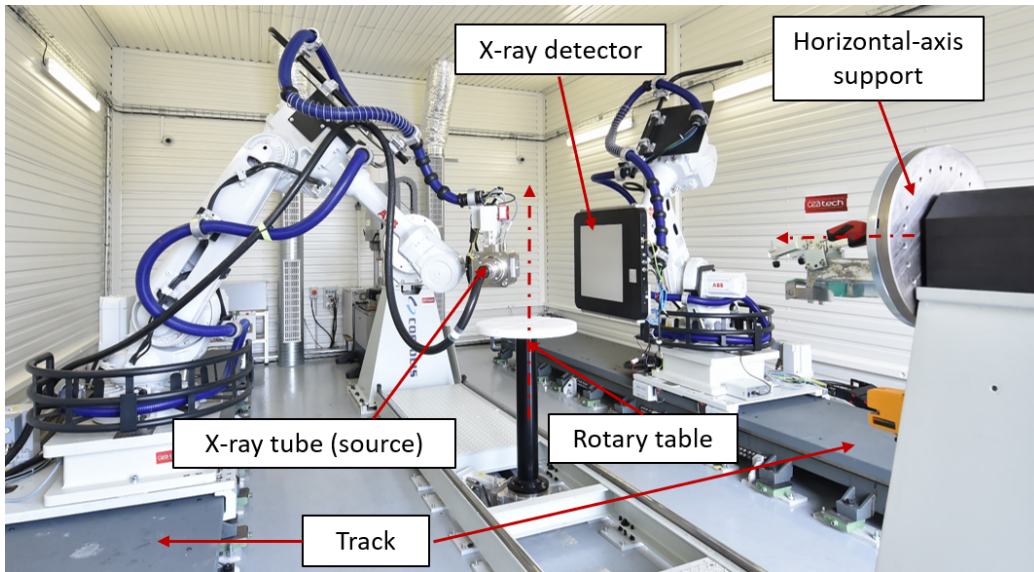


Figure 3: Robotised X-ray imaging platform ELIXIR - The positioning on the rotary table is not studied within this work. We address the problematic of high-dimensional parts located on the horizontal axis support (Fig.17).

express regret that no measurements in using real scan data have been performed yet. Additionally, they emphasize the need of calibration methods to compensate for the robot absolute positioning errors [17]. Different methods have been proposed to improve positioning performance such as on-line positioning adaptation with external tools (laser-tracker) or modelings that account for the transient changes due to environmental factors or robot self-heating (thermal effect) [18].

The novelty of this work lies in a methodology (See Figure 4) that combines different tools. The first one improves the absolute accuracy of the robot by identifying thermal drift and backlashes [18] (1). The second one, using an original calibration phantom named the calibration comb and placed on the detector allows us to have a good understanding of the source in relation to the detector (2). Finally, a large-sized phantom is designed to calibrate source and detector positions in the cell frame. This device also enables a clear definition of the rotation axis of the part to be reconstructed (3). To highlight the quality of our work, we evaluate the raw process capability and the contribution of each method.

To evaluate the process capability, reconstruction criteria are defined ac-

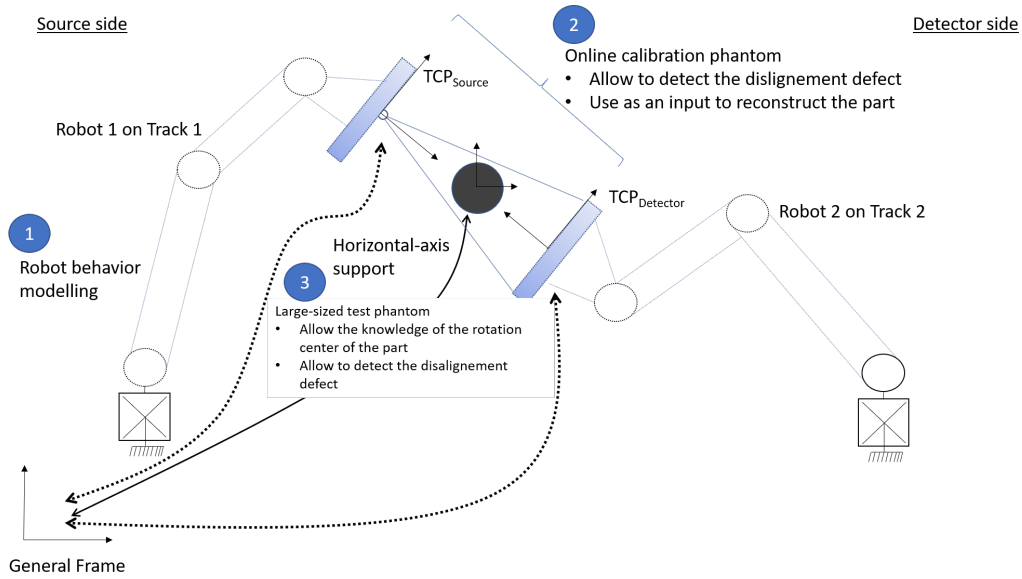


Figure 4: Process capability measurement methodology

cordingly to the controlled object. The size of inner defects such as porosity or cracks represents one reconstruction criterion. Another criterion is the reconstruction accuracy of specific geometrical objects. In this case, following the literature, sphere objects [19] are used to assess the quality of reconstruction with key performance indicators including radius, sphere-to-sphere distances and mean sphericity errors.

The work is organised as follows: in Section II, we evaluate the capability of the robotic cell and its impact on part reconstruction. Section III is dedicated to the three strategies. Section IV and V deal with the discussion, the conclusion and providing perspectives.

2. Raw process capability

The raw process capability involves measuring the capability of the robotized XCT. After evaluating the robot positioning performances, we assess the influence of positioning errors in two configurations. In the first one, these errors serve as input for the numerical reconstruction of spheres. This quantitative assessment of the degradation of reconstructed volumes is used as a reference to evaluate the relevance of the methods presented in Section 3. In the second configuration, we qualitatively demonstrate the effect of

raw process capability on the detectability of porosity defects in a composite industrial part.

2.1. Robot positioning measurement

To simplify the study, the robot positioning accuracy is evaluated on a linear trajectory along x axis without displacement of the robot basis on the track. The study is performed on one robot and the method is applied to the second one. The displacement involves stretching and bending the robot arm (Figure 5). The positioning accuracy is assessed at multiple positions along the trajectory using laser-tracker measurement which provide Tool Center Point (TCP) positions in the cell frame after processing. The measured positions are then compared to programmed ones, as illustrated in Figure 6. The results reveal substantial accuracy errors between the programmed (orange) and measured (blue) trajectories. The maximal positioning error Δr_i in each axis is then identified as follows:

$$\Delta r_i = \max |i_m - i_p|, \quad i = \{x, y, z\} \quad (1)$$

where i_m and i_p are respectively the measured and programmed positions.

The values Δr_x , Δr_y and Δr_z are estimated:

- $\Delta r_x = 0.24 \text{ mm}$
- $\Delta r_y = 0.38 \text{ mm}$
- $\Delta r_z = 0.72 \text{ mm}$

These results highlight the approximate sizes of positioning errors that can be anticipated in the context of X-ray source and detector positioning.

2.2. Modeling of the geometrical configuration

The effect of the positioning uncertainty, as determined by previous measurement, is studied in circular XCT simulations. The quality of reconstruction relies on a precise estimation of the geometrical configuration (Figure 7) which is defined through nine parameters describing the positioning of source and detector:

- f is the distance between the source and the principal point U_0 which is the orthogonal projection of the source onto the detector plane

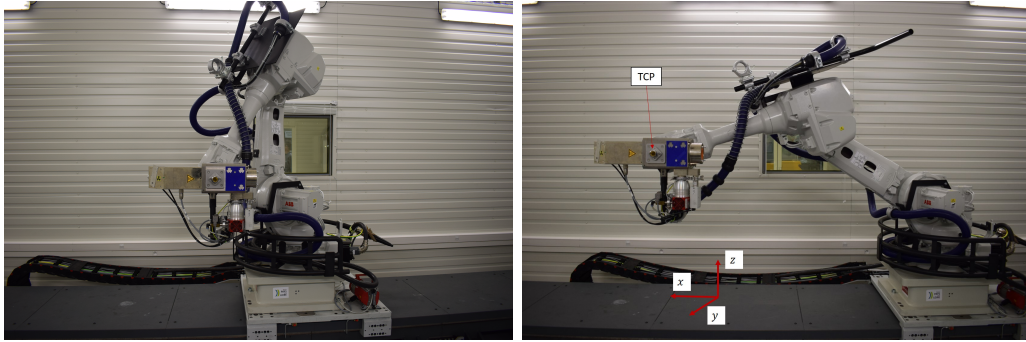


Figure 5: Linear trajectory measurement from folded (a) to stretched (b) arm configurations

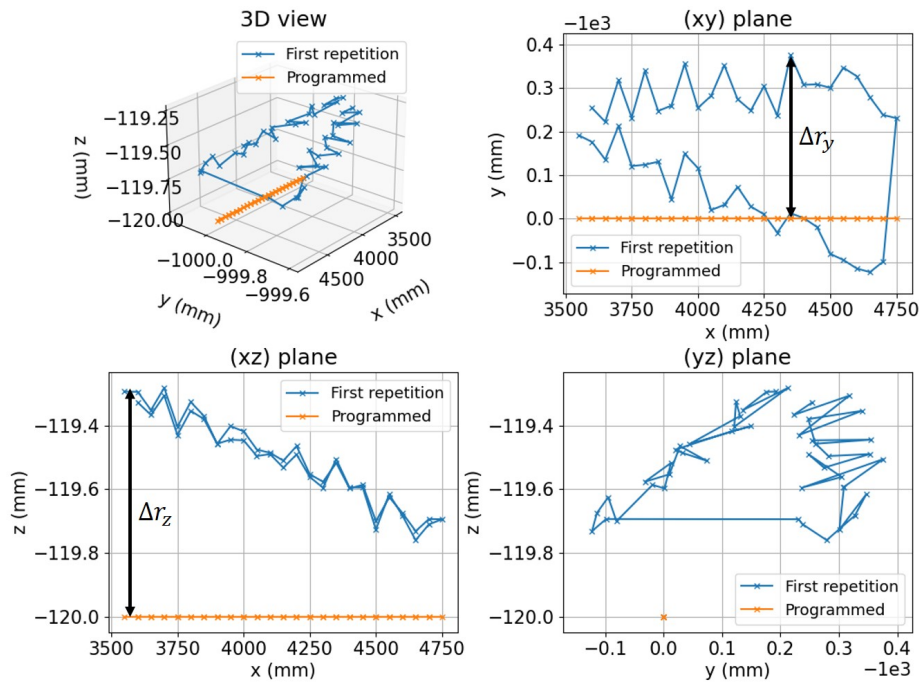


Figure 6: Comparison between measured and programmed trajectory: 3D view and Cartesian projections

- u_0, v_0 are the coordinates of the principal point U_0 in the detector frame

- θ, η, ϕ are the detector angles with reference to the world coordinate frame (axes x, y, z) for a ZYX Euler convention
- t_1, t_2, t_3 are the source coordinates with reference to the world coordinate frame

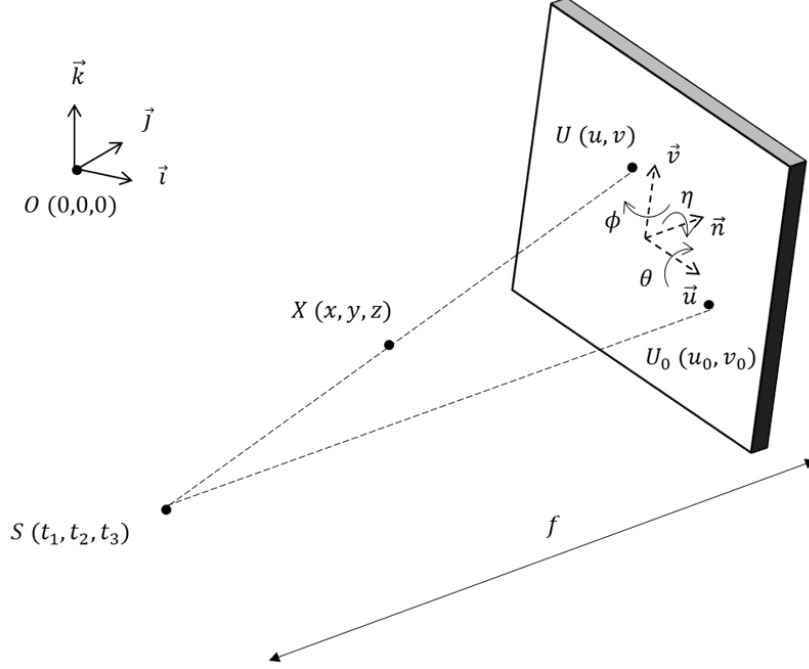


Figure 7: Geometrical configuration of detector and source positions and orientation

This approach allows us to evaluate u_0, v_0, f, t_1, t_2 and t_3 within the range of $\Delta r_x, \Delta r_y$ and Δr_z to estimate the reconstruction errors. Since the orientation errors of robot positioning can not be directly obtainable from measurement, we utilize a modified Denavit-Hartenberg model (DHm) [20] to calculate these values based on the robot geometry. The position ${}^0X_{TCP}$ and orientation ${}^0R_{TCP}$ of the end-effector are defined using the homogeneous transformation matrix ${}^0T_{TCP}$ as follows :

$${}^0T_{TCP} = \begin{bmatrix} {}^0R_{TCP} & {}^0X_{TCP} \\ 0 & 1 \end{bmatrix} \quad (2)$$

Where:

$${}^0T_{TCP} = \prod_{i=0}^n {}^{i-1}T_i(q_i, a_i, d_i, \alpha_i, \theta_i) \quad (3)$$

With $a_i, d_i, \alpha_i, \theta_i$ the geometrical parameters of the DHm and q_i the joint angles.

DH parameters are determined through a least-square resolution that minimizes residuals between the model and measured positions. Using Eq. 2 and 3, the homogeneous transformation matrix ${}^0T_{TCP}$ is computed for every position along the trajectory, utilizing the identified DHm parameters. As a result, the rotation matrix ${}^0R_{TCP}$ is extracted and Euler angles θ, η and ϕ are determined such as:

$${}^0R_{TCP} = R_z(\phi)R_y(\eta)R_x(\theta) \quad (4)$$

The orientation errors are then determined similarly to Equation 1 with $i = \{\theta, \eta, \phi\}$. The resulting maximal orientation errors are:

- $\Delta r_\theta = 0.13^\circ$
- $\Delta r_\eta = 0.15^\circ$
- $\Delta r_\phi = 0.11^\circ$

To this extent, the influence on the quality of reconstruction can be evaluated afterwards.

2.3. Influence of positioning errors on the quality of reconstruction

The object under study is a simulated test phantom in which 3 mm diameter steel balls are placed along a spiral depicted in Figure 8. Steel balls are commonly used as reference reconstruction objects. Radiographs of the phantom are simulated using the attenuation Beer-Lambert law (Equation 5 and 9) for the ideal geometrical configuration (Table 1) and a 2048×2048 pixels detector with a pixel size $T_{pixel} = 0.200$ mm.

$$I = I_0 \exp(-\mu L) \quad (5)$$

with I the absorbed energy, I_0 the initial energy, μ the steel attenuation linear coefficient and L the crossed length of steel.

Reconstruction is performed using FBP algorithm [21] implemented in the RTK Python package [22] and leads to a voxel size of 0.133 mm.

This configuration corresponds to a standard X-ray source and detector positioning in a circular XCT with a reasonable magnification (1.5).

The methodology used to measure the effect of geometrical parameters errors on the quality of spheres reconstruction follows these steps :

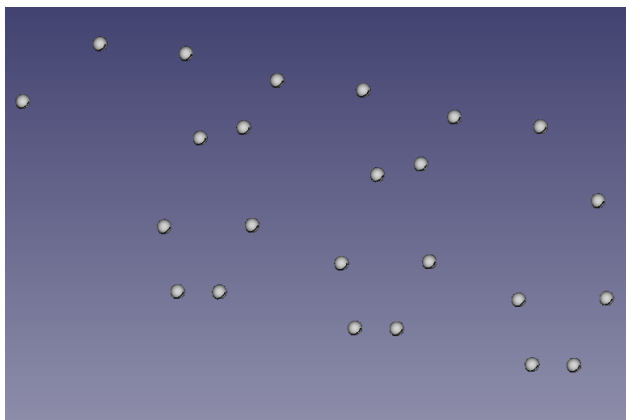


Figure 8: Simulation of a test phantom with balls steel

| f | u_0 | v_0 | θ | η | ϕ | t_1 | t_2 | t_3 |
|--------|-------|-------|----------|--------|--------|-------|---------|-------|
| 600.00 | 0.00 | 0.00 | 0.00 | 0.00 | 0.00 | 0.00 | -400.00 | 0.00 |

Table 1: Ideal configuration geometrical parameters: lengths are in mm and angles in $^\circ$

- The acquisition of 360 radiographs of the balls phantom is performed using an attenuation Beer-Lambert model with the ideal geometrical configuration.
- An offset to one of the nine parameters is applied based on the previous estimated positioning errors.
- The reconstruction is performed using FBP algorithm.
- An empirical threshold is applied to the volume slices to select the voxels corresponding to the balls. This threshold has been determined for the ideal geometry reconstruction which leads to the optimal reconstruction quality.
- 3D clustering of the corresponding balls regions is performed.
- Each group of cloud points is fitted to a sphere with a least-square resolution by optimizing radius r and center position (x_c, y_c, z_c) to minimize residuals between the cloud points and the virtual sphere. Three sphere properties are then determined: sphere center, sphericity error (mean error between cloud points and the fitted sphere) and radius error (difference between actual and measured radius). From the spheres center

positions, the distances to closest spheres are computed and compared to the theoretical ones to calculate the sphere-to-sphere distance errors.

Figure 9 provides an example of inaccurate geometry estimation in the reconstruction of spheres. The reconstruction with actual parameters results in satisfactory spheres identification, but the introduction of positioning errors affects the spheres properties. This approach enables us to quantitatively link positioning errors with the geometrical quality of the reconstruction.

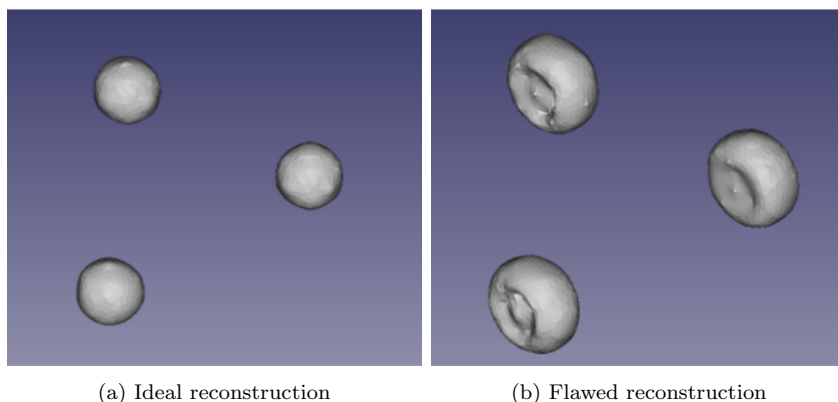
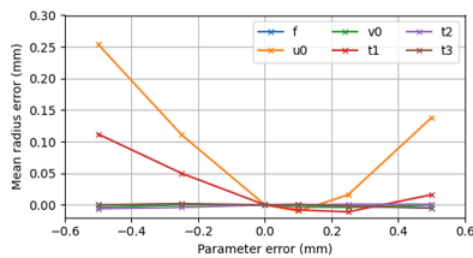


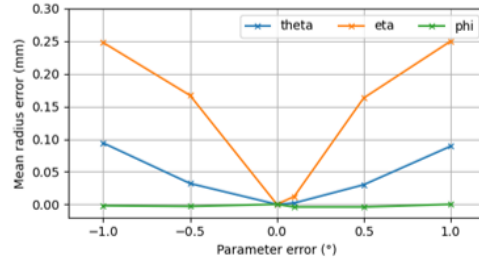
Figure 9: Reconstructed spheres after image thresholding

Positioning errors have been previously estimated at up to 0.5 mm for length parameters and 0.15° for angle parameters. The latter have been increased to 1.0° to study a wider range. Geometrical parameters are studied independently to observe the critical impact of each one on the reconstruction criteria. Therefore, each simulation pertains to a single parameter error to avoid coupled effects. The results are summarized in Figure 10 which includes mean radius, sphere-to-sphere distance and sphericity errors for both length and angle parameters. An overall substantial difference in the quality of reconstruction is observed based on these parameters. Notably, the parameters u_0 and t_1 corresponding to horizontal shifts of source and detector are the most critical for the quality of sphere reconstruction as they significantly increase the radius and sphericity errors. Indeed, a 0.5 mm error on u_0 leads to 0.25 mm radius error while magnification and vertical parameters barely affects sphere reconstruction properties. Orientation errors also deform the spheres shape. The in-plane angle η has a more significant impact than the out-of-plane angles θ and ϕ as it increases errors in all three reconstruction criteria. The effect is approximately three times stronger for the in-plane

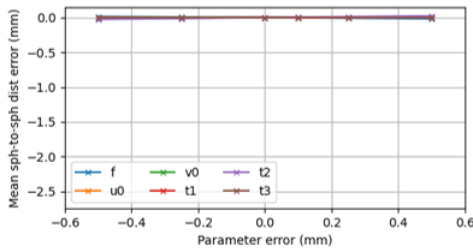
angle. The out-of-plane ϕ angle (rotation around vertical axis z) has no influence on the reconstructed spheres. In the most critical configuration, the radius errors reach up to 0.25 mm . This value is substantial compared to the nominal radius value (1.5 mm), highlighting the strong deformation of spheres shape.



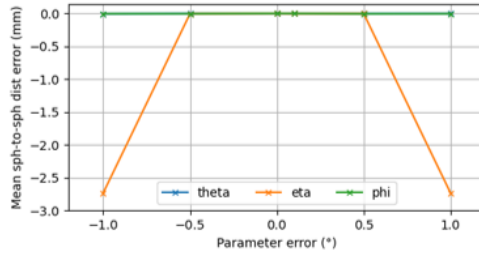
(a) Mean radius errors for lengths parameters



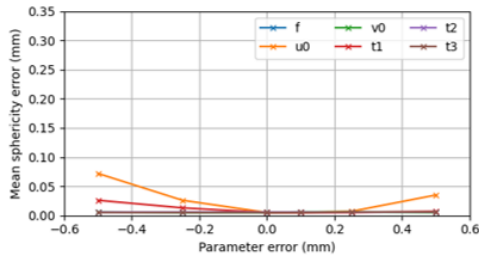
(b) Mean radius errors for angles parameters



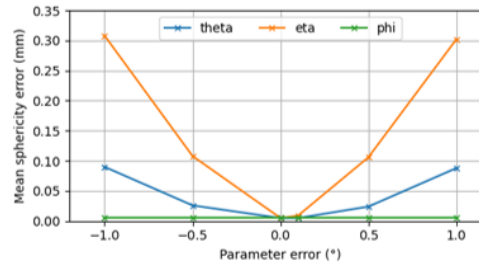
(c) Mean sphere-to-sphere distance errors for lengths parameters



(d) Mean sphere-to-sphere distance errors for angles parameters



(e) Mean sphericity errors for lengths parameters



(f) Mean sphericity errors for angles parameters

Figure 10: Reconstruction errors for lengths and angles parameters errors

To sum up, for a configuration with a voxel size of 0.133 mm , robot positioning errors can lead to a degradation of reconstruction quality.

2.4. Direct reconstruction of an industrial composite part with inner defects

A complementary study of the raw process capability is conducted on an industrial composite part exhibiting porosities. In this case, the quality criteria are the detectability of inner defects. The experimental setup is as follows: the source and detector are positioned on both sides of the part, which is placed on a rotating table for this recording of projections. Consequently, the positioning effect is taken into account. Two reconstructions are computed: one with the theoretical parameters resulting from the programmed positions and the second one with the parameters identified to improve the quality of reconstruction. Comparison between both reconstructed volumes highlights the effect of raw process capability on the detection of defects such as porosity or inclusions (Figure 11). Indeed, the calibrated reconstruction (b) allows for slice visualization, enabling the detection of a porosity with a maximum length of 4.5 *mm*. However, this defect is not discernible by the reconstruction resulting from programmed positions as artifacts obscure the reconstructed volume.

The study of raw process capability through the measurement of robot positioning accuracy and the reconstruction of specific shapes or industrial parts has highlighted the sensitivity of a standard circular XCT to geometrical errors. The magnitudes of undetected defects sizes or shape deformations are linked to robot accuracy, which is especially influenced by the trajectory and the tomography configuration. The latter is primarily defined by the magnification ratio, which in turn modifies the voxel size. It is within this framework that three main strategies are investigated to enhance the capability of the XCT robotic cell.

3. Improvement methods of X-ray tomography process capability

Three different methods are investigated to enhance the process capability. In each case, the steel ball phantom is used to assess the enhancement of reconstruction quality. Advantages, drawbacks and usage conditions are also presented. Table 3 provides a summary of the properties of the reconstructed spheres for the three methods.

3.1. Thermo-geometrical robot model

A relevant information of the study of raw process capability is the significant impact of accuracy errors on the tomography process. Improving the

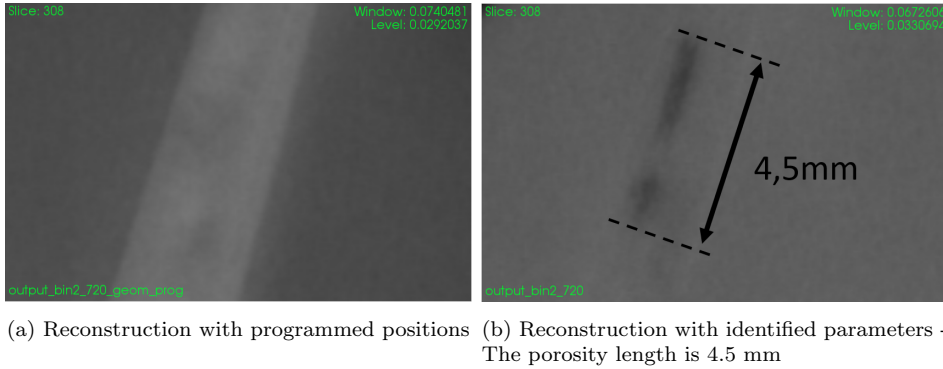


Figure 11: Zooms on porosity defect in a slice of the reconstructed volumes

robot behavior model is a way of limiting robot positioning errors. Here, a corrective method is employed, focusing on the compensation of the thermal drift and the backlash effect, which can respectively negatively affect repeatability and bidirectional accuracy. The backlash effect is highlighted in Figure 6 with the gap between forwards and backwards paths. A thermo-geometrical model adapted from DHm is defined. Optimization of the parameters enables a significant reduction in the effects of backlash and thermal drift [18]. The obtained results underline that achieving an accuracy close to the repeatability of the robot is achievable. In this way, the residual maximal accuracy errors in each direction are (Figure 12):

- $\Delta r_x = 0.091 \text{ mm}$
- $\Delta r_y = 0.075 \text{ mm}$
- $\Delta r_z = 0.096 \text{ mm}$

Similarly to Section 2.3, these errors are input into the reconstruction algorithm to evaluate the deformation of the reconstructed spheres.

3.2. Implementation of an online calibration phantom

This method leans on the fastening of a calibration phantom to the detector. It theoretically enables an online calibration. For a non-standard trajectory such as limited-view-angle tomography which requires displacements of source and detector around the Region of Interest (ROI), a calibration phantom fixed to the detector enables to calibrate source positions

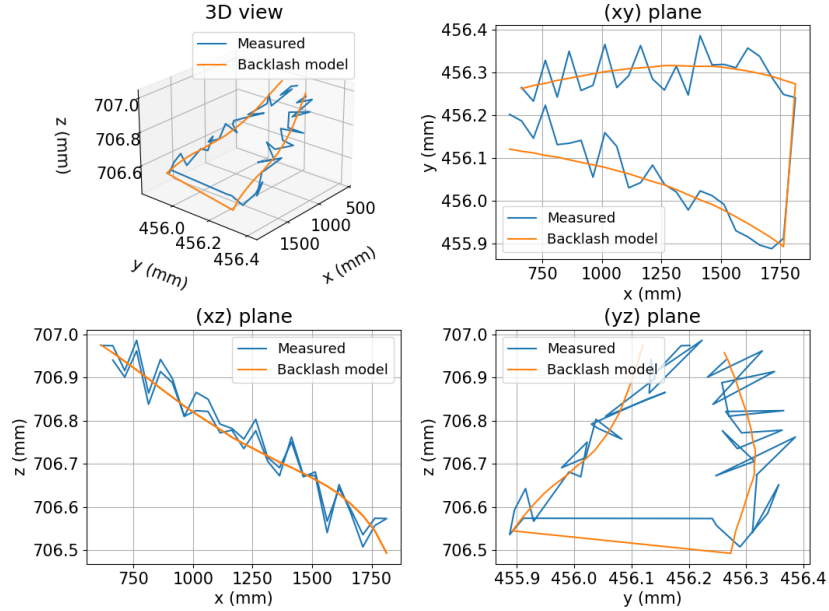


Figure 12: Calibration of DHm robot

which respect to the detector. In each position, a unique radiograph is performed containing the ROI of the controlled part and the projection of the calibration phantom. Features of the ROI and phantom must not overlap. As a result, the area dedicated to the controlled part is reduced. However, this method is not time consuming as it does not require to replace the part with a standard calibration phantom. Moreover, each position is calibrated independently.

The device is called the "calibration comb". The comb, as illustrated in Figure 13, is an experimental sample manufactured by electrical discharge machining with a teeth width of 0.51 mm . A calibration comb consists of a regular alternation of teeth and gaps, whose geometry is precisely known. The principle is similar to a vernier scale in a caliper. Based on the geometry of the comb, *i.e.* teeth width, and the geometrical configuration, the projection of the comb onto the detector produces a specific pattern. Figure 14 illustrates an experimental configuration with a radiograph of the comb. The theoretical pattern projection is depicted in Figure 15. The objective is that

the teeth shadows T_{zone} length is superior to the pixel size T_{pixel} , defined by the fraction x such as:

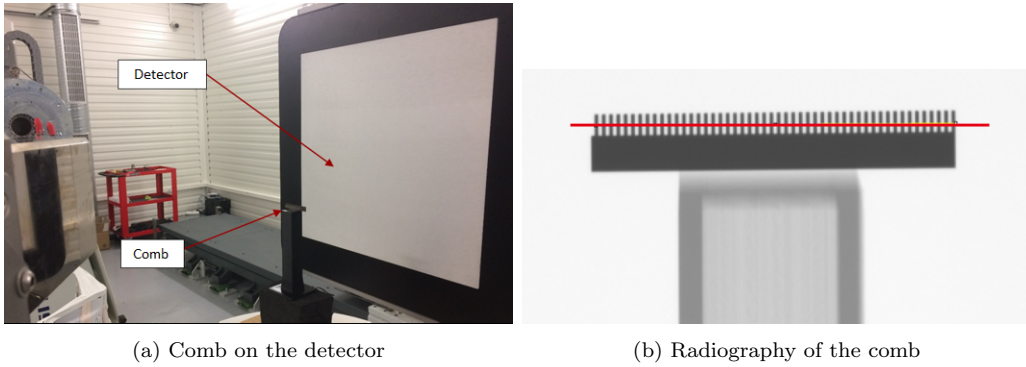
$$x = \frac{T_{zone}}{T_{pixel}} \quad (6)$$

Figure 15 gives an example of a fraction of $x = 1.1$. First pixel absorbs 100%, second one 90%, third 20%, and so on. Spatial derivation of this raw signal leads to a nearly-sinusoidal function with one predominant frequency f_x . We demonstrate that f_x is correlated to x such as:

$$f_x = \frac{1}{10x} \quad (7)$$



Figure 13: Calibration comb prototype with 0.51 mm teeth width



(a) Comb on the detector

(b) Radiography of the comb

Figure 14: Radiography of the comb

The signal phase is measured by fitting a sinusoidal function (Figure 16(a)). A first calibration of the signal reference is performed to measure the signal phase ϕ_r in a configuration where the source is perfectly aligned

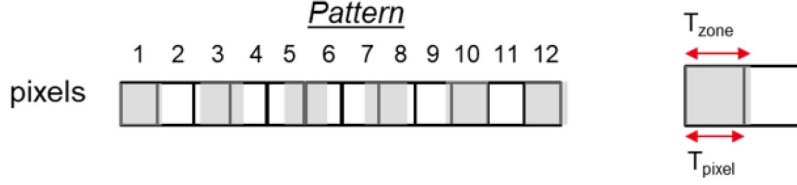


Figure 15: Theoretical projection of calibration comb. Teeth shadows are little larger than pixel size. Here is an example where $x = \frac{T_{zone}}{T_{pixel}} = 1.1$.

with the detector center. The signal phase for the actual configuration ϕ_a is determined to compute the phase difference $\Delta\phi$. The calibration consists of measuring the phase difference to estimate the detector shift u_0 or v_0 .

Simulations were carried out on a numerical comb to establish the function between signal phase difference $\Delta\phi$ and geometrical misalignments u_0 (horizontal detector axis) or v_0 (vertical detector axis). Figure 16(b) displays the signal phase difference as a function of horizontal offset u_0 . The blue cross points correspond to the signal phase difference measurement on numerical signals. The evolution is fitted by a linear regression:

$$\Delta\phi = ku_0 \quad (8)$$

with: $k = -76.6^\circ/mm$

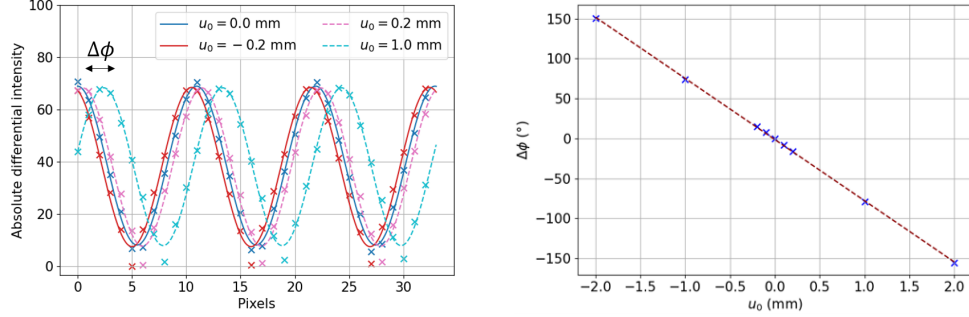
A signal analysis sensitivity study estimated the phase difference uncertainty measurement: $\phi_{unc} = \pm 2.5^\circ$. This value leads to source-to-detector-center offsets uncertainty : $u_{0,unc} = v_{0,unc} = \pm 0.03 mm$.

Reconstruction simulations are conducted using raw source-to-detector-center offsets accuracy errors and calibrated offsets to evaluate the effectiveness of the calibration comb. The calibration comb reduces the reconstruction spheres errors, as mean radius and sphericity errors decrease respectively from 0.093 to 0.016 mm and 0.013 to 0.001 mm.

This numerical study underlines the enhancement offered by such a calibration phantom which can significantly reduce horizontal and vertical source-to-detector-center misalignments.

3.3. Large-sized steel balls calibration phantom

The online calibration comb has demonstrated its potential to reduce errors on two parameters of the geometrical configuration such as the horizontal and vertical source-to-detector-center misalignments. However, the



(a) Phase difference for several horizontal offsets u_0 (b) Signal phase difference - horizontal offset graph

Figure 16: Signal analysis of the comb phantom simulations with a geometrical configuration corresponding to a signal frequency $F = 0.909 \text{ pixels}^{-1}$

raw process capability study has underlined the potential impact of other parameters, particularly orientation errors. Therefore, a method based on a standard balls calibration phantom [23] has been explored and adapted to the specific requirements of a large robotized XCT cell. This type of calibration phantom relies on the perfect knowledge of spheres centers $X(x, y, z)$ in the cell frame (Figure 17). It involves capturing radiographs of a sufficient number of balls where the radiograph displays ellipses corresponding to the projection of the balls (Figure 18). These ellipses are then processed to calculate the projection centers $U(u, v)$ which corresponds to the projection of the ball centers. These points X and U are related through a pin-hole camera model:

$$sU = SR(X - T) \quad (9)$$

with:

$$S = \begin{bmatrix} f & u_0 & 0 \\ 0 & 1 & 0 \\ 0 & v_0 & 0 \end{bmatrix} \quad (10)$$

$$R = R_z(\phi)R_y(\eta)R_x(\theta) \quad (11)$$

$$R = \begin{bmatrix} c_\phi c_\eta & -s_\phi c_\theta + c_\phi s_\eta s_\theta & s_\phi s_\theta + c_\phi s_\eta c_\theta \\ s_\phi & c_\phi c_\theta + s_\phi s_\eta s_\theta & -c_\phi s_\theta + s_\phi s_\eta c_\theta \\ -s_\eta & c_\eta s_\theta & c_\eta c_\theta \end{bmatrix} \quad (12)$$

$$T = \begin{bmatrix} t_1 \\ t_2 \\ t_3 \end{bmatrix} \quad (13)$$

where $s_i = \sin(i)$ and $c_i = \cos(i)$.



Figure 17: Large-sized test phantom installed

The calibration consists of minimizing the objective function g which calculates the difference between measured U_{exp} and model U_{mod} projection centers by optimizing the geometrical parameters \mathbf{p} .

$$g(\mathbf{p}) = \sum \|U_{exp} - U_{mod}(\mathbf{p})\| \quad (14)$$

where U_{mod} are calculated following Equation 9.

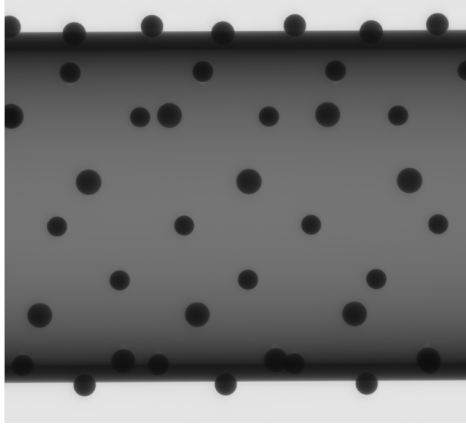


Figure 18: Example of a radiography of the large-sized steel balls calibration phantom. Centres of the ellipses are determined after image processing.

The quality of geometrical calibration strongly depends on a precise understanding of the positions of the center of the balls. This is why a metrological control and an identification of the phantom origin and orientation with respect to the cell frame are necessary to accurately determine the position of the balls in the cell frame. After minimization of the objective function, the identified geometrical parameters must match the actual geometrical configuration. To account for the uncertainty of the metrological control and the phantom frame identification, denoted as Δx_{unc} , a Monte-Carlo simulation is performed to estimate the resulting uncertainty in the geometrical parameters. The features of the simulation are as follows :

- Number of simulations: $N = 1000$
- Number of balls: $M = 43$
- Uncertainty of balls positions: $\Delta x_{unc} = \pm 0.032 \text{ mm}$

The distributions of the identified geometrical parameters are illustrated in Figure 19. A D'Agostino and Pearson test [24] is conducted to check the normality of the distributions, which enables the computation of $1-\sigma$ and $3-\sigma$ probability intervals corresponding to 68% and 99% respectively. Table 2 summarizes the $1-\sigma$ and $3-\sigma$ uncertainties of geometrical parameters. The $3-\sigma$ uncertainty is used as an input to the reconstruction algorithm to evaluate the effect of residuals errors on the quality of sphere reconstruction.

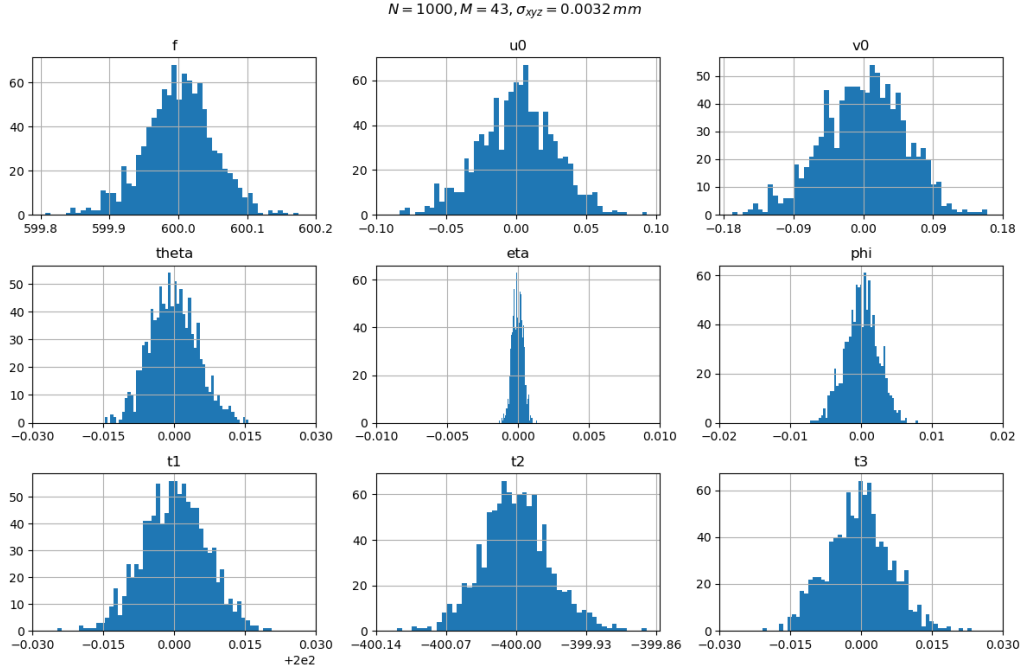


Figure 19: Distributions of identified parameters over $N = 1000$ simulations. The length and angles parameters are respectively expressed in mm and $^\circ$.

The results are presented in Table 3, where we compare all the methodologies and showcase the improvements achieved in terms of accuracy.

| Interval | f | u_0 | v_0 | t_1 | t_2 | t_3 | θ | η | ϕ |
|-------------|-------|-------|-------|-------|-------|-------|----------|--------|--------|
| | (mm) | | | | | | (°) | | |
| 1- σ | 0.049 | 0.026 | 0.055 | 0.007 | 0.033 | 0.007 | 0.005 | 0.000 | 0.002 |
| 3- σ | 0.147 | 0.079 | 0.164 | 0.020 | 0.099 | 0.020 | 0.015 | 0.001 | 0.007 |

Table 2: Parameters uncertainty at 1- σ and 3- σ

4. Discussion

The first section underscores the concerns regarding a large-sized robotized XCT cell. The precise control of robot positioning is essential to ensure the highest quality tomography, whether it involves standard circular, helical, or non-standard trajectories. Such platforms are designed to handle large,

complex-shaped parts. Helical and limited-view-angle trajectories align with the capabilities of the cell, which utilizes two industrial robots and one automated system specifically designed for handling long parts. These types of tomography require the source and detector to move on both sides of the part. The quality of reconstruction is significantly impacted by errors in estimating the geometrical configuration. Therefore, an inaccurate understanding of the geometrical configuration, caused by errors in robot positioning or the absence of correction, becomes critical for the relevance of tomographic control.

Three complementary methods have been investigated to enhance the process capability. For simplicity, the improvement possibilities offered by these methods are evaluated in a standard circular tomography configuration. Each method reduces reconstruction errors but also presents advantages and drawbacks.

According to the authors, the thermo-geometrical model is the first method to consider since it requires no additional work during the tomographic process and can be executed within the development time frame of the platform. The primary drawback is the requirement for specific equipment, such as a laser tracker, to calibrate the model.

Additionally, two calibration methods have been introduced, both relying on the measurement of geometrical positioning errors. The calibration comb is particularly useful in the context of non-standard tomography, which involves multiple source and detector positions, and consequently, robot displacements. It offers the advantage of online calibration, as no further manipulation is required. Indeed, it consists of capturing the features of the comb and the controlled part in a single radiograph. However, a limitation of this method is that a portion of the radiograph must be allocated to the comb, reducing the available space for the controlled part. Despite this drawback, the method allows for the calibration of two parameters, the effects of which on the reconstruction process have been emphasized.

The third method involves the use of a standard ball calibration phantom, which has been adapted to meet the cell size requirements. This phantom allows for the calibration of all geometrical parameters and significantly reduces reconstruction errors. In the case of a circular trajectory without robot displacement, radiographs of the phantom are captured after the part inspection. However, for helical or limited-view-angle tomographies, multiple source and detector positions are required. In this method, the trajectory is repeated after inspecting the part to calibrate each position. Consequently,

the calibration accuracy depends on the repeatability of the robots, which is, however, closely aligned with the remaining uncertainty provided by the calibration. In all configurations, this method exhibits high efficiency potential but is more time-consuming. Additionally, it requires a budget for manufacturing and controlling the phantom.

Finally, to assess the performance of metrological tools, specifically X-Ray Computed Tomography systems [25], ISO 14253–1:2017 [26] and the International Vocabulary of Metrology (VIM) [27] define MPE as the ‘Extreme value of measurement error, with respect to a known reference quantity value, permitted by specifications or regulations for a given measurement, measuring instrument, or measuring system.’ In our case, we defined this error as the mean error plus three standard deviations. Consequently, our relatively independent test results reveal the following outcomes: a maximum error of 0.020 *mm* for the radius and 0.015 *mm* for the sphere-to-sphere distance.

| Simulation | Radius error (<i>mm</i>) | | Sphere-to-sphere distance error (<i>mm</i>) | | Mean sphericity error (<i>mm</i>) |
|---------------------|----------------------------|-------|---|-------|-------------------------------------|
| | Mean | Std | Mean | Std | |
| Raw accuracy errors | 0.051 | 0.022 | 0.033 | 0.003 | 0.012 |
| Robot model | 0.017 | 0.001 | 0.007 | 0.001 | 0.001 |
| Calibration comb | 0.016 | 0.001 | 0.012 | 0.001 | 0.001 |
| Large-sized phantom | 0.015 | 0.001 | 0.011 | 0.001 | 0.001 |

Table 3: Properties of the reconstructed spheres with raw process and improvement methods capabilities

5. Conclusion and perspectives

Robotized X-ray tomography has demonstrated its potential in inspecting volumetric defects in large-dimensional parts. The process quality relies heavily on the precision of robot positioning. We assessed the raw process capability through simulations with a standard circular tomography using a ball phantom and practical applications on industrial parts. Both approaches underscored the impact of robot positioning accuracy on the reconstructed volume.

To enhance process capability, we explored three complementary methods: a thermo-geometrical robot model, the implementation of an online calibration phantom and a large-sized steel ball calibration phantom. Each

method exhibited the potential to improve reconstruction quality in standard circular tomography, offering distinct advantages and applications. We validated the theoretical improvements through simulations.

Furthermore, we discussed the applicability of these methods in non-standard trajectory XCT applications, highlighting specific advantages and drawbacks. Importantly, these methods can be implemented concurrently. Our future objectives include the complete experimental validation of these methods and their application in limited-view-angle and helical XCT trajectories.

The reconstruction of large parts deformed under their own weight is also an important issue to deal with, as the parts' geometries may differ from their natural shape.

Another perspective is the thermal instrumentation of the robots to update the thermo-geometrical model in real-time. The objective is to avoid a lengthy warming phase that may be required to reach a stable thermal state. Enhancing the prediction offered by the thermo-geometrical model would improve the repeatability of the robot on long trajectories, bringing it closer to its nominal repeatability.

Acknowledgments

This research work is funded by the Conseil Régional des Pays de la Loire.

Competing interests

The authors declare none.

References

- [1] M. Krumm, C. Sauerwein, V. Hämmerle, S. Heile, T. Schön, A. Jung, M. Sindel, Rapid robotic x-ray computed tomography of large assemblies in automotive production, in: Proceedings of the 8th Conference on Industrial Computed Tomography (iCT 2018), Wels, Austria, 2018, pp. 6–9.
- [2] P. J. Withers, C. Bouman, S. Carmignato, V. Cnudde, D. Grimaldi, C. K. Hagen, E. Maire, M. Manley, A. Du Plessis, S. R. Stock, X-ray computed tomography, *Nature Reviews Methods Primers* 1 (1) (2021) 1–21.

- [3] C. Yu, J. Xi, Simultaneous and on-line calibration of a robot-based inspecting system, *Robotics and computer-integrated manufacturing* 49 (2018) 349–360.
- [4] J. A. Hashem, M. Pryor, S. Landsberger, J. Hunter, D. R. Janecky, Automating high-precision x-ray and neutron imaging applications with robotics, *IEEE Transactions on Automation Science and Engineering* 15 (2) (2017) 663–674.
- [5] M. Lüthi, B. A. Bircher, F. Meli, A. Küng, R. Thalmann, X-ray flat-panel detector geometry correction to improve dimensional computed tomography measurements, *Measurement Science and Technology* 31 (3) (2019) 035002.
- [6] M. Ferrucci, W. Dewulf, A. Dönmez, Measurement of sample stage error motions in cone-beam x-ray computed tomography instruments by minimization of reprojection errors, *Precision Engineering* 67 (2021) 48–57.
- [7] W. Holub, F. Brunner, T. Schön, Roboct-application for in-situ inspection of joint technologies of large scale objects, in: Fürth (Germany): International Symposium on Digital Industrial Radiology and Computed Tomography, 2019.
- [8] P. Landstorfer, J. Hiller, M. Herbst, Investigation of positioning accuracy of industrial robots for robotic-based X-ray computed tomography (2019) 5.
- [9] L. De Chiffre, S. Carmignato, J.-P. Kruth, R. Schmitt, A. Weckenmann, Industrial applications of computed tomography, *CIRP annals* 63 (2) (2014) 655–677.
- [10] G. Herl, J. Hiller, M. Thies, J.-N. Zaech, M. Unberath, A. Maier, Task-specific trajectory optimisation for twin-robotic x-ray tomography, *IEEE Transactions on Computational Imaging* 7 (2021) 894–907.
- [11] D. Evangelista, M. Terreran, A. Pretto, M. Moro, C. Ferrari, E. Menegatti, 3d mapping of x-ray images in inspections of aerospace parts, in: 2020 25th IEEE International Conference on Emerging Technologies and Factory Automation (ETFa), Vol. 1, IEEE, 2020, pp. 1223–1226.

- [12] F. Bauer, D. Forndran, T. Schromm, C. U. Grosse, Practical part-specific trajectory optimization for robot-guided inspection via computed tomography, *Journal of Nondestructive Evaluation* 41 (3) (2022) 1–23.
- [13] C. Doignon, B. Maurin, B. Bayle, M. de Mathelin, A visual 3d-tracking and positioning technique for stereotaxy with ct scanners, *Robotics and Autonomous Systems* 56 (5) (2008) 385–395.
- [14] Product specification - IRB 4600 (2020).
- [15] H. Banjak, X-ray computed tomography reconstruction on non-standard trajectories for robotized inspection, Ph.D. thesis, Université de Lyon (2016).
- [16] J. Hiller, P. Landstorfer, P. Marx, M. Herbst, Evaluation of the impact of faulty scanning trajectories in robot-based x-ray computed tomography, *Measurement Science and Technology* 32 (1) (2020) 015401. doi:10.1088/1361-6501/abaf2a.
URL <https://doi.org/10.1088/1361-6501/abaf2a>
- [17] G. Herl, J. Hiller, A. Maier, Scanning trajectory optimisation using a quantitative tuybased local quality estimation for robot-based x-ray computed tomography, *Nondestructive Testing and Evaluation* 35 (3) (2020) 287–303.
- [18] A. Le Reun, K. Subrin, A. Dubois, S. Garnier, Thermal drift and backlash issues for industrial robots positioning performance, *Robotica* (2022) 1–20.
- [19] M. Ferrucci, E. Ametova, S. Carmignato, W. Dewulf, Evaluating the effects of detector angular misalignments on simulated computed tomography data, *Precision Engineering* 45 (2016) 230–241.
- [20] J. Denavit, R. S. Hartenberg, A kinematic notation for lower-pair mechanisms based on matrices (1955).
- [21] L. A. Feldkamp, L. C. Davis, J. W. Kress, Practical cone-beam algorithm, *Journal of the Optical Society of America A* 1 (6) (1984) 612. doi:10.1364/JOSAA.1.000612.

URL <https://www.osapublishing.org/abstract.cfm?URI=josaa-1-6-612>

- [22] S. Rit, M. Vila Oliva, S. Brousmiche, R. Labarbe, D. Sarrut, G. C. Sharp, The Reconstruction Toolkit (RTK), an open-source cone-beam CT reconstruction toolkit based on the Insight Toolkit (ITK), *Journal of Physics: Conference Series* 489 (2014) 012079. doi:10.1088/1742-6596/489/1/012079.
URL <https://iopscience.iop.org/article/10.1088/1742-6596/489/1/012079>
- [23] M. Ferrucci, R. K. Leach, C. Giusca, S. Carmignato, W. Dewulf, Towards geometrical calibration of x-ray computed tomography systems—a review, *Measurement Science and Technology* 26 (9) (2015) 092003. doi:10.1088/0957-0233/26/9/092003.
URL <https://iopscience.iop.org/article/10.1088/0957-0233/26/9/092003>
- [24] E. S. Pearson, R. B. D’Agosteno, K. O. Bowman, Tests for departure from normality: Comparison of powers, *Biometrika* 64 (1977) 231–246.
- [25] E. Zwanenburg, M. Williams, J. Warnett, Performance testing of dimensional x-ray computed tomography systems, *Precision Engineering* (2022).
- [26] A. Balsamo, et al., Geometrical product specifications (gps)—inspection by measurement of workpieces and measuring equipment—part 5: Uncertainty in verification testing of indicating measuring instruments (2015).
- [27] A. Balazs, International vocabulary of metrology-basic and general concepts and associated terms, *Chemistry International* 25 (2008).